Electromagnetic control of the instability in the liquid metal flow over a backward-facing step

Ya-Dong Huang(黄亚冬)[1,2], Jia-Wei Fu(付佳维)[2], and Long-Miao Chen(陈龙淼)[2,†]

[1] *Jiangsu University, Zhenjiang* 212013, *China*
[2] *Nanjing University of Science and Technology, Nanjing* 210094, *China*

(Received 1 July 2022; revised manuscript received 25 September 2022; accepted manuscript online 10 October 2022)

The tile-type electromagnetic actuator (TEA) and stripe-type electromagnetic actuator (SEA) are applied to the active control of the perturbation energy in the liquid metal flow over a backward-facing step (BFS). Three control strategies consisting of base flow control (BFC), linear model control (LMC) and combined model control (CMC) are considered to change the amplification rate of the perturbation energy. CMC is the combination of BFC and LMC. SEA is utilized in BFC to produce the streamwise Lorentz force thus adjusting the amplification rate via modifying the flow structures, and the magnitude of the maximum amplification rate could reach to 6 orders. TEA is used in LMC to reduce the magnitude of the amplification rate via the wall-normalwise Lorentz force, and the magnitude could be decreased by 2 orders. Both TEA and SEA are employed in CMC where the magnitude of the amplification rate could be diminished by 3 orders. In other words, the control strategy of CMC could capably alter the flow instability of the liquid metal flow.

Keywords: electromagnetic actuator, backward-facing step flow, flow instability, flow control

PACS: 47.20.–k, 47.85.L– **DOI:** 10.1088/1674-1056/ac989d

1. Introduction

The liquid metal is widely utilized in the thermal management and energy storage due to its high thermal conductivity,[1,2] such as heat exchange in nuclear engineering,[3] cooling of high-power-density microdevices,[4] and harvesting the low grade heat to generate electricity.[5] Also, the liquid metal is attractive in the mechanical to electrical energy conversion via magneto-hydrodynamics (MHD) generator[6] due to its excellent electoral conductivity. In the heat transfer flow system, both the heat transfer efficiency and the flow instability are commonly taken into consideration. Usually, a backward-facing step (BFS) is designed in the heat exchanger to enhance the heat transfer via flow separation and reattachment.[7,8] The BFS flow often contains two separation bubbles and the flow structures are mainly dependent on the Reynolds numbers based on the maximum inlet velocity and the hight of the step.[9] Perturbations could gain energy amplification when flowing through the separation bubbles owing to the Kelvin–Helmholtz (KH) instability,[10] Taylor–Görtler instability,[11] centrifugal instability[12] and other instability mechanisms,[13,14] and the amplification may make a great influence on the heat transfer efficiency.[15,16] Thereby, researchers adopt active[17,18] and passive[19,20] controls of the BFS flow to achieve the desired heat transfer efficiency. However, the perturbation amplification may aggravate the flow system instability, which is unfavourable for the liquid metal transport. It is an available strategy that the control method could regulate the perturbation energy in the liquid metal BFS flow.

As a classical law of physics, the interactions between the electrical current and the magnetic field in the liquid metal could generate the Lorentz force to control the flow[21,22] and transport the liquid metal.[23] In former studies, the Lorentz force had made great contributions to drag reduction, transition suppression and so forth in the flow control. The Lorentz force is generated by the electromagnetic field which could be excited via the electromagnetic actuator consisting of alternatively arranged electrodes and magnetic poles, and having two types: tile and stripe.[24] The tile-type electromagnetic actuator (TEA) and stripe-type electromagnetic actuator (SEA) could engender the wall-normal and wall-parallel Lorentz force respectively. It was found the streamwise (or wall-parallel) Lorentz force applied in the separation bubble could reduce the bubble size thus modifying the growth rates of the perturbation energy.[25] Moreover, the perturbation energy in the BFS flow also could be adjusted by the linear control model with a feed-forward controller.[26,27] Although research has proposed several control methods to adjust the instability in the BFS flow, the flexibility for different control strategies needs further discussion. Hence, the control effects of different control strategies on the instability in the liquid metal BFS flow would be investigated in this paper.

†Corresponding author. E-mail: chenlongmiao@njust.edu.cn
© 2022 Chinese Physical Society and IOP Publishing Ltd

2. Methodology

The incompressible liquid metal flow controlled via the Lorentz force is modelled by the Navier–Stokes equation:

$$\partial_t \boldsymbol{u} + \boldsymbol{u}\cdot\boldsymbol{\nabla}\boldsymbol{u} = -\boldsymbol{\nabla}p + Re^{-1}\boldsymbol{\nabla}^2\boldsymbol{u} + \boldsymbol{f}, \tag{1a}$$

$$\boldsymbol{u} = \boldsymbol{U} + \boldsymbol{u}', \tag{1b}$$

$$p = P + p', \tag{1c}$$

$$\boldsymbol{f} = \boldsymbol{F} + \boldsymbol{f}', \tag{1d}$$

where $(\boldsymbol{U}, P)$ are the base flow variables and $(\boldsymbol{u}', p')$ are the perturbation variables. $\boldsymbol{F}$ is the Lorentz force controlling the base flow. The base flow is described by the following equation:

$$\partial_t \boldsymbol{U} + \boldsymbol{U}\cdot\boldsymbol{\nabla}\boldsymbol{U} = -\boldsymbol{\nabla}p + Re^{-1}\boldsymbol{\nabla}^2\boldsymbol{U} + \boldsymbol{F}, \tag{2}$$

while the linear evolution of perturbations can be predicted by solving the following linear perturbation equation:

$$\partial_t \boldsymbol{u}' + [\boldsymbol{U}\cdot\boldsymbol{\nabla} + (\boldsymbol{\nabla}\boldsymbol{U})^{\mathrm{T}}\cdot]\boldsymbol{u}' = -\boldsymbol{\nabla}p' + Re^{-1}\nabla^2\boldsymbol{u}' + \boldsymbol{f}'. \tag{3}$$

The source force $\boldsymbol{f}'$ could be considered as

$$\boldsymbol{f}' = \mathcal{F}_q q + \mathcal{F}_\vartheta \vartheta, \tag{4}$$

containing the external forcing term $\mathcal{F}_\vartheta\vartheta$ and the Lorentz force $\mathcal{F}_q q$. $\mathcal{F}_q$ and $\mathcal{F}_\vartheta$ are the spatial structures of the body force, and q and ϑ are time-dependent variables representing the noise source and control input respectively.

According to the achievements in Refs. [25,26], three control strategies: the base flow control (BFC), linear model control (LMC) and their combination (combined model control, CMC) are considered to adjust the flow instability in this paper. The control model is shown in Fig. 1. The step height is h which is also the characteristic length. The height of the expansion channel is $2h$. To be convenient for description and calculation, the origin of the Cartesian coordinate locates on the step corner. As the Reynolds number in current research is 500, the uncontrolled steady flow contains the primary separation bubble (PSB) on the lower wall and the secondary separation bubble (SSB) on the upper wall. x_1 is the reattachment point of PSB, and x_2, x_3 are the separation and reattachment points of SSB.

It could be observed that three electromagnetic actuators (A_1, A_2, and A_3) and two sensors (S_1 and S_2) exist in the flow system. According to our previous investigation,[25] SEAs A_1 and A_2 could be installed inside the separation bubbles in BFC. TEA A_3 is applied to LMC which also has the sensors S_1 and S_2. The sensor S_1 is placed near the noise source to measure the incoming disturbance because ϑ is very difficult to come by in physical experiments. The sensor S_2 is employed to measure the outputs.

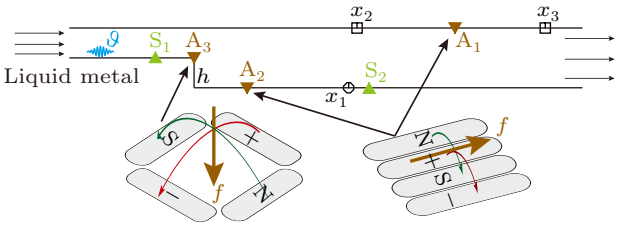


Fig. 1. Control model.

In LMC and CMC, the linear control model could be established based on the numerical data of Eq. (2) via the Galerkin projection. As the BFS flow usually acts as a noise amplifier, the Galerkin-based method has many limitation in accurately capturing the transfer behavior from the input to the output. Some researchers adopted the auto-regressive moving-average exogenous (ARMAX) model[28] to perform the system identification. For simplicity, researchers usually formulate the state-space system in a discrete-time format. The mapping of the inputs s, q from S_1, A_3, and the output m from S_2 could be described by the following model:

$$\underbrace{m_n + \sum_{k=1}^{n_a} a_k m(n-k)}_{1} = \underbrace{\sum_{k=n_{dq}}^{n_{bq}+n_{dq}} b_k^q q(t-k)}_{2} + \underbrace{\sum_{k=n_{ds}}^{n_{bs}+n_{ds}} b_k^s s(t-k)}_{3} + \underbrace{\sum_{k=1}^{n_c} c_k e(n-k) + e_n}_{4}, \tag{5}$$

where m is the output and term 1 is the auto-aggressive part. q and s are the inputs and terms 2,3 represent the exogenous part. e is the noise and term 4 means the moving average part. The coefficients a_k, b_k, and c_k could be found via regression. n_a is the previous outputs on which the current output depend on. n_{dq} and n_{ds} represent the numbers of the passed inputs due to the delaying effects of the input on the output. n_{bq} and n_{bs} mean the numbers of the previous inputs on which the current output depends. n_c is the number of time-colored noise. Readers could know more about the detailed meaning of the parameters in Eq. (5) in Ref. [26].

In BFC and CMC, the sphere of action is set as $0 < x/h < 8$ for A_2 and $10 < x/h < 15$ for A_3 according to the bubble scale. Meanwhile, the streamwise Lorentz force generated by SEA could be approximately written as $N\mathrm{e}^{-5\pi d}$ [29] where N is the control number and d is the distance to the SEA surface which could be considered as the upper/lower wall. In LMC and CMC, the wall-normalwise Lorentz force which satisfies the Gaussian distribution[30] also could be considered the control input in the linear control model. Then, the location of

sensors S_1, S_2 and the spatio-temporal characteristics of ϑ and the wall-normalwise Lorentz force from A_3 are identical to those reported in Ref. [31].

3. Mesh and validation

All equations are solved with a high accuracy spectral-element method (SEM)[32] in the domain shown in Fig. 2. The spatial domain is split into 2039 quadrilateral finite elements, in which both the geometry and solution variables employ equal-order tensor-product Lagrange polynomial expansions. The flow separates near the corner of the step and the circumfluence in the separation bubbles generates near the upper and lower walls, so the grids there are refined. Gauss–Lobatto Legendre polynomials are adopted as a basis for the numerical solution. The time-stepping method based on the backwards-time differencing[33] is taken to perform the time integration. The Krylov subspace method and the Arnoldi decomposition method are employed to solve the eigenvalue in the optimal transient growth analysis.

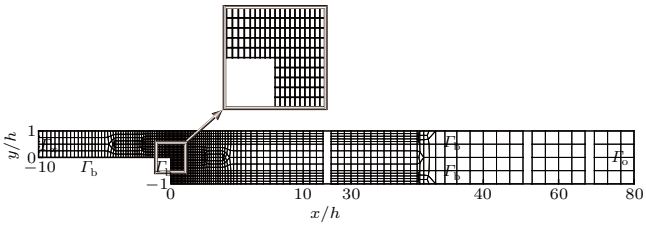


Fig. 2. Calculation domain and mesh.

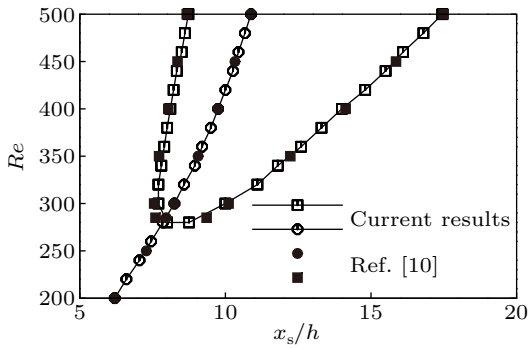


Fig. 3. Separation bubble length varying with the Reynolds numbers from references and current results.

For the base flow solution, a Dirichlet condition is set at $\Gamma_\infty(U = 4y - 4y^2, V = 0)$, and a Neumann condition is set at $\Gamma_o(\nabla_n U = 0, \nabla_n V = 0)$. A no-slip Dirichlet condition is set at $\Gamma_b(U = 0, V = 0)$. A high-order Neumann condition for the normal component along the boundary calculated from Eq. (1) is set for the pressure at all boundaries except Γ_o where the pressure is set to be zero. For the linear stability analysis, the boundary conditions are similar with those in the base flow solution, but the perturbation velocity $\boldsymbol{u}'$ is set to be zero at Γ_∞ and Γ_b. For the optimal transient growth analysis, perturbations at all boundaries are set to be zero. Besides, readers cloud learn more about the detailed solution procedure of the eigenproblem in the optimal transient growth analysis via the achievements of Barkley *et al.*[33] In all calculations, the time-step is set as 0.001 with the second-order time integration and eighth-order polynomials. The lengths of the primary and secondary separation bubbles x_s as a function of Reynolds number are shown in Fig. 3. Both lengths increase with the Reynolds number, and our results are consistent with those in the reference.

4. Results and discussion

4.1. Effects of BFC

The maximum amplification rates G_m of the initial Gaussian perturbation ϑ as well as the corresponding steady base flow with BFC are reported in Fig. 4. N_1 and N_2 represent the control numbers of the streamwise Lorentz force from A_1 and A_2 respectively. N_1 and N_2 constitute the coordinate system of control numbers. It is worth mentioning that the inlet noise source in BFC is also the noise source $\mathcal{F}_\vartheta \vartheta$ in LMC and CMC. In BFC, we mainly discuss the control effects based on the single initial wall-normalwise perturbation. In order to facilitate our research, it is assumed that the noise source obeys the Gaussian distribution, which could be written as

$$\mathcal{F}_\vartheta = A \exp\left(\frac{-(x-x_0)^2}{2\sigma_x^2}\right) \exp\left(\frac{-(y-y_0)^2}{2\sigma_y^2}\right), \tag{6}$$

where A is the amplitude of perturbations, (x_0, y_0) is the center of perturbations and σ_x, σ_y are the radiation radii of perturbations. The parameter in Eq. (6) are $(x_0, y_0) = (-0.5, 0.25)$, $(\sigma_x, \sigma_y) = (0.1, 0.1)$, and $A = 4.0$, and the perturbation variable ϑ could be expressed via the Dirac function.

It could be observed that G_m could achieve the peak value at $(0.1, 0.2)$ while the minimal one at $(0.15, 0)$ according to Fig. 4(a). Meanwhile, the distributions of G_m also illustrate that the streamwise Lorentz force only acting on SSB could reduce the maximum amplification rate, while acting on both PSB and SSB could achieve the opposite effects. In other words, it could stabilize the liquid metal flow via fixing SEA only in SSB, or destabilize the flow by setting SEA in both separation bubbles. Figure 4(b) demonstrates the steady base flows of which the maximum amplification rates are marked in Fig. 4(a). Cases A–E correspond to the control numbers at $(N_1, N_2) = (0, 0)$, $(0.15, 0)$, $(0.3, 0)$, $(0.3, 0.2)$, and $(0.1, 0.2)$ respectively. The contour in Fig. 4(b) is colored by the streamwise velocity. The solid blue lines represent the isolines of $U = 0$, and the liquid metal inside the isoline contains a backflow. Moreover, the isolines also present the scales of the separation bubbles. We can clearly see the PSB and SSB for the no-control (NC) case (case A). For case B, there only exists the PSB but its length is larger than that for case A because the streamwise Lorentz force could reduce the magnitude of

the backflow velocity of the separation bubble, and then the bubble dwindles gradually. The decrease of SSB size may flatten the concave streamline near SSB, and then the separation streamline near PSB may lift up. Once the control strength from A_1 increases (case C), the length of PSB might take a growth. If the electromagnetic actuator A_2 is turned on, the PSB could be divided into two smaller bubbles (case D). However, the scale of PSB in the wall-normalwise direction is much larger than that of SSB, so effects of the streamwise Lorentz force on SSB size are more remarkable. It could be observed that the scale of the downstream divided bubble might be reduced once the control strength from A_2 decreases by comparing cases D and E. It is obvious that the amplification rate of the initial Gaussian perturbation energy is minimal for case B and maximum for case E.

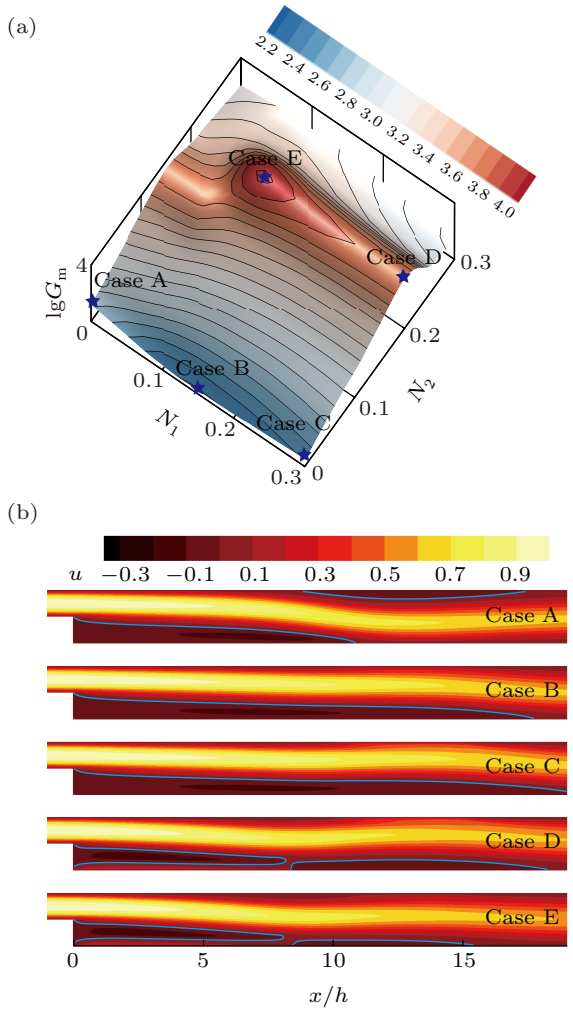


Fig. 4. The maximum growth rates of the initial Gaussian perturbation for different control numbers and corresponding base flows. (a) The maximum growth rates. (b) The corresponding base flow.

Figure 5 shows the energy derivative varying with the time calculated from the Reynolds–Orr equation.[34] The energy derivative is nondimensionalized by E_0/t_0 where E_0 is the initial perturbation energy and t_0 is the unit time. Actually, $\mathrm{d}E/\mathrm{d}t$ has a positive correlation to the rates of the curves in Fig. 4, and $G(t)$ in Fig. 4 achieves the peak value at the time corresponding to $\mathrm{d}E/\mathrm{d}t = 0$ in Fig. 5.

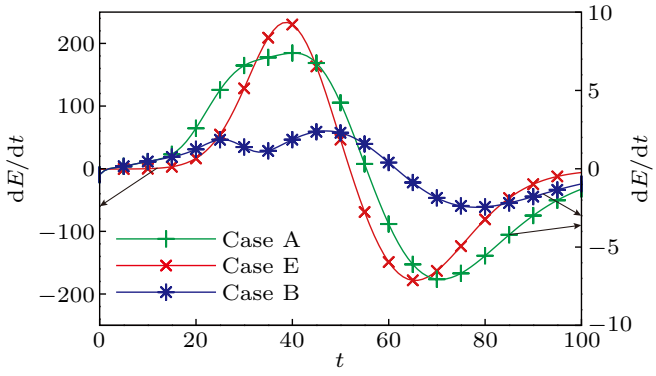


Fig. 5. Growth rate of perturbation energy varying with the evolution time.

Figure 6(a) shows the optimal energy growth of perturbations over a given time interval τ. It is the fact that the peak amplification rate of the perturbation energy in the optimal transient growth is much larger than that of the single initial Gaussian perturbation. We know that the optimal initial perturbations in the optimal transient growth are different and they are dependent on the time interval. It could be found that the optimal amplification rate of the two-dimensional perturbation always increases with the evolution interval and reaches to the peak value at about $\tau = 60$, and then decays. Figure 6(b) presents the optimal initial perturbations of which the optimal amplification rates at $\tau = 60$ are shown in Fig. 6(a). The perturbation energies are normalized, and the contours are colored with the perturbation vorticity of the level from -0.1 to 0.1. The patterns of the optimal initial perturbations resemble the KH vortices, and always distribute along the separation line. The typical spatial distribution like the KH vortices in the optimal initial perturbation could diminish the effects of distortion and dissipation from the mean strain field because each initial perturbation could evolve into the KH-like vortices.

Figure 7 illustrate the optimal amplification rates of the three-dimensional perturbations for the evolution interval of $\tau = 60$ and corresponding optimal initial perturbations. The optimal amplification rate of the three-dimensional perturbation energy slightly increases at small spanwise wavenumbers, and then decreases. The maximum value approximately appears at $\beta = 0.5$. The magnitude of the optimal amplification rate in case E is still the maximum one while that in case B is always the minimal one for the same spanwise wavenumber. This phenomenon indicates that BFC assurely increase or decrease the amplification rate of the perturbation energy in the liquid metal BFS flow. The three-dimensional optimal initial perturbation is visualized via the spanwise velocity. The distributions of the three-dimensional optimal initial perturbations are different from the two-dimensional ones. Besides the step corner and the outlines of the separation bubbles, most

spanwise perturbations locate near the step. This distribution features are similar with those in Ref. [10].

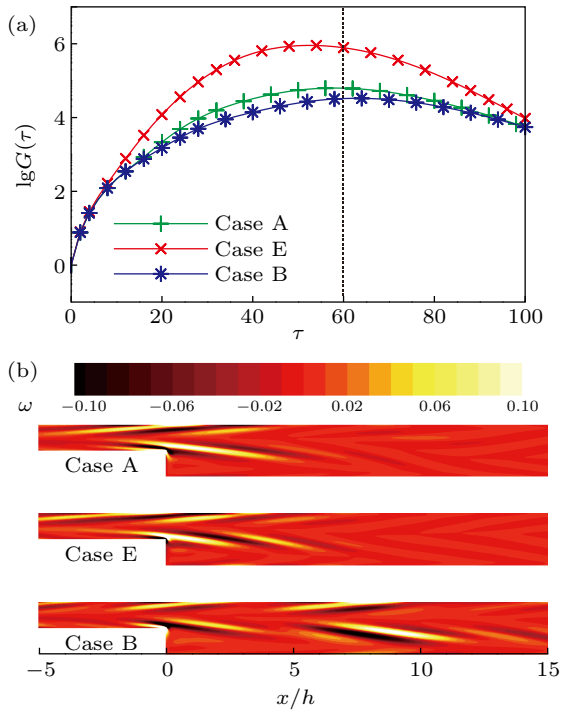


Fig. 6. The optimal amplification rate of two-dimensional perturbations and corresponding initial perturbations. (a) Optimal amplification rates varying with the evolution intervals; (b) corresponding initial perturbations.

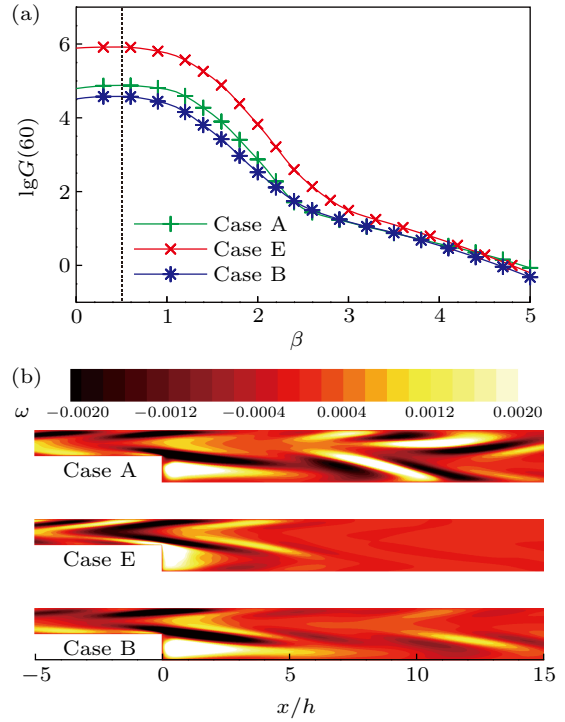


Fig. 7. The optimal amplification rate of three-dimensional perturbations and corresponding initial perturbations. (a) Optimal amplification rates varying with the spanwise wave numbers; (b) corresponding initial perturbations.

4.2. System identification in LMC and CMC

The above discussions have indicated that BFC could capably modify the perturbation energy in the liquid metal BFS flow. However, the flow system needs to keep laminar sometimes since the liquid metal contains a high heat transfer efficiency. The perturbation energy also could be amplified in BFC, thereby LMC and CMC are adopted to suppress the amplification of the perturbation energy in our control strategies. Certainly, CMC also could be employed to increase the perturbation energy because it contains BFC. It is noteworthy that LMC and CMC are performed based on cases A and B respectively. For contrast, the spatial distribution of the noise source ϑ in LMC and CMC is same with that in BFC, and the Lorentz force from the actuator A_3 also has the Gaussian distributions, and the parameters of $\mathcal{F}_q$ from A_3 are $(x_0, y_0) = (-0.05, 0.01)$, $(\sigma_x, \sigma_y) = (0.01, 0.1)$, and $A = 4.0$. Meanwhile, the perturbation variable ϑ could be expressed as the Gaussian white noise with the standard deviation of 0.01 and the control input q could be written as the binary random function with the maximum amplitude of 0.0054 like Ref. [10].

Usually, referred to Ref. [31], the sensor S_1 is located downstream the noise source but upstream the actuator A_3, and the sensor S_2 is placed near the reattachment point of PSB, thereby the signals of input and output in LMC and CMC are defined as follows:

$$s = \int_{-0.25}^{-0.35} \frac{\partial u'}{\partial y} \mathrm{d}\Gamma, \tag{7a}$$

$$m = \begin{cases} \displaystyle\int_{10.9}^{11} \frac{\partial u'}{\partial y} \mathrm{d}\Gamma \ \text{(for LMC)}, \\ \displaystyle\int_{17.8}^{17.9} \frac{\partial u'}{\partial y} \mathrm{d}\Gamma \ \text{(for CMC)}. \end{cases} \tag{7b}$$

Figure 8(a) shows the amplitude-frequency characteristics of the original input and output signals in CMC. In order to reflect the amplification features of the flow system on the noise, the signals s and m here are obtained without the control input signal q. It can be seen that the amplitude of all signals attenuates rapidly when the frequency is greater than 1, so the low-pass filter could be adopted to extract the main parts of signals. The principle of the low-pass filtering is keeping the low-frequency amplitude-frequency characteristics as well as the amplitude of the original input and output signals. The transfer function of the low-pass filtering here is referred to Ref. [31] and could be written as

$$\boldsymbol{T}(\mathfrak{s}) = \frac{\omega_c^2}{\mathfrak{s}^2 + 2\eta\omega_c\mathfrak{s} + \omega_c^2} \tag{8}$$

with $\eta = 0.8$ and $\omega_c = 2$. Figure 8(b) shows the amplitude-frequency characteristics of the low-pass filtered signal. It can be seen that the filtered signals has the similar amplitude-frequency characteristics with the original signals. In addition, the amplitude–frequency characteristics of the original and low-pass filtered signals with the same transfer function in LMC also resemble those in Fig. 8.

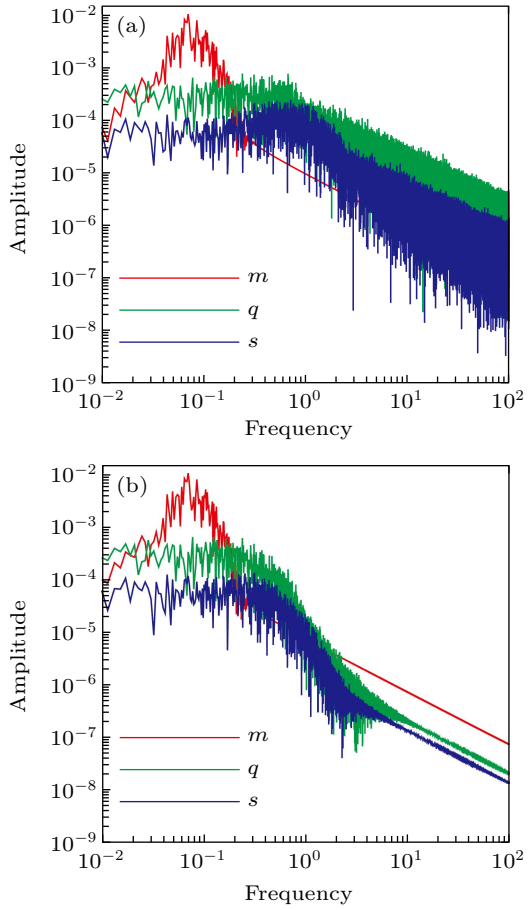


Fig. 8. Amplitude–frequency characteristics of original and filtered signals. (a) Original signal; (b) filtered signal.

Although the amount of data in the control model needs to be reduced, it is still necessary to ensure that the sampling data is sufficient. As mentioned above, the time step is 0.001 in all calculations, so the sampling period is set to 0.1. Figure 9 shows the auto-correlation and cross-correlation functions between the sampling signals. Observing the auto-correlation function curve of the output signal m, it could be seen that the curve reaches the minimum value at the time of $t = 4.1$ and $t = 6.0$ for LMC and CMC respectively. That is to say, there might be a duration of 4.1 and 6.0 for the previous outputs having an impact on the subsequent outputs. Hence, the value of n_a in the ARMAX models for LMC and CMC are $4.1/0.1 = 41$ and $6.0/0.1 = 60$ respectively. In addition, the cross-correlation function curves of s and m, q, and m begin to fluctuate intensely at $t = 11.5$ for LMC and $t = 22.5$ for CMC. This phenomenon demonstrates the response delay time of the output to a single input is 11.5 and 22.5 for LMC and CMC respectively, so the values of n_{ds} and n_{dq} in the ARMAX model should be around 115 for LMC and 225 for CMC. Once the cross-correlation function curves (green one) of q and m take an intense fluctuation, the time intervals between the first wave valley and wave peak are 2.9 and 4.2 for LMC and CMC respectively. This appearance indicates that the time interval of the input signal affecting the current output is 2.9 for LMC and 4.2 for CMC. Thereby, the value of n_{bq} in the ARMAX model is around 29 for LMC and 42 for CMC. In fact, as S_1 is close to A_3, the value of n_{bq} is similar with that of n_{bs} in the ARMAX model.

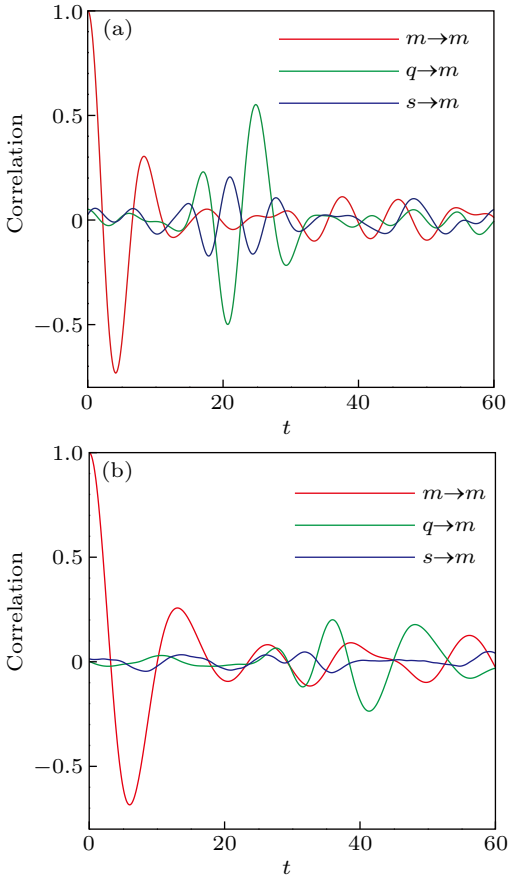


Fig. 9. Auto-correlation and cross-correlation characteristics of the measured variables. (a) LMC; (b) CMC.

The parameters in the ARMAX models for LMC and CMC are shown in Table 1. The primary sharp of signals predicted by the ARMAX model are mostly dependent on these parameters. n_a, n_{bq}, n_{bs}, n_{dq}, and n_{ds} are usually determined firstly and then n_c is adjusted to improve the goodness of fit between the predicted and sampling signals. The goodness of fit could be expressed as

$$\text{fit} = 1 - \frac{\|m_\text{p} - m_\text{r}\|_2}{\|m_\text{r}\|_2} \times 100\%, \tag{9}$$

where m_p is the signal predicted by the ARMAX model and m_r is the sampling signal. Figure 10 shows the predicted and sampling signals. It could be observed that the output signals from the ARMAX model coincide with the sampling signals. The goodness of the fit is 91.2% and 86.4% for LMC and CMC respectively.

Table 1. Parameters in the ARMAX model.

	n_a	n_{bq}	n_{bs}	n_{dq}	n_{ds}	n_c	fit (%)
LMC	41	29	29	112	120	8	91.2
CMC	60	42	42	228	229	11	86.4

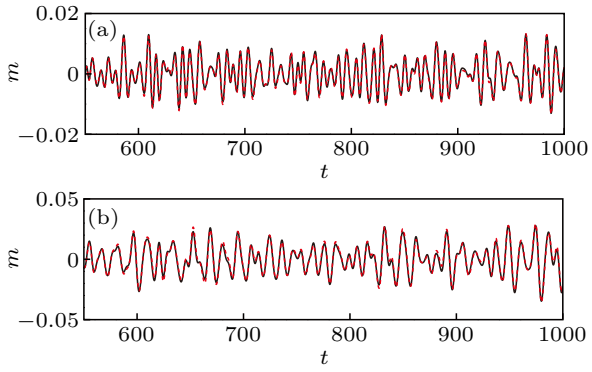


Fig. 10. The signals predicted by the ARMAX model (black line) and the sampling signals (red line). (a) Signals in LMC. (b) Signals in CMC.

Figure 11 shows the impulse response of the output signal to a single input signal in the ARMAX model. As discussed above, the start time of response has been shown in Table 1. For LMC, the amplitude of the response signal tends to 0 when $t > 35$, while it still has slight fluctuations when $t > 65$ and tends to 0 until $t > 110$ for CMC. It could be found that the two response signals for each control strategy fluctuate in opposite directions. The time for the output response to the noise signal achieving the peak value slightly lags behind the response to the control input signal, because the actuator A_3 is downstream the sensor S_1. Comparing the maximum amplitudes of the response signals, we could observe that the peak amplitude of the response to the noise signal is greater than that of the response to the control input signal both for LMC and CMC, because the spatial distribution area of the noise source signal is larger than that of the control input signal.

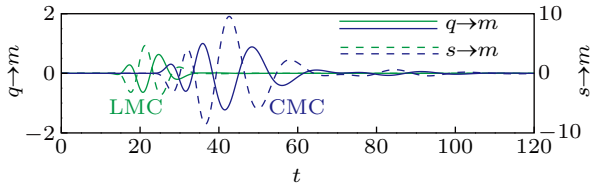


Fig. 11. The characteristics of impulse response in the ARMAX model.

4.3. Closed-loop control in LMC and CMC

Once the parameters of the ARMAX model are achieved, the transfer functions of $q \to m$ and $s \to m$ are identified. The coefficients in the transfer function are referred as the Markov parameters, which represent the impulse response of the system. If we want to know the future control signal according to the measured signal, the corresponding compensator needs to be designed to build a complete closed-loop system. The system without compensator is called an open-loop system. The relationship between the future output signal $\boldsymbol{M}_T$, the known (or measured) noise signal $\boldsymbol{S}^g$, the control signal $\boldsymbol{Q}^g$ and the future unknown control signal $\boldsymbol{Q}^f$ could be constructed via the Markov matrices $\boldsymbol{Z}_s$, $\boldsymbol{Z}_q$, and $\boldsymbol{L}_q$ in any sampling time period T. The expression could be written as

$$\begin{aligned}\underbrace{\begin{pmatrix} m_n \\ m_{n+1} \\ \vdots \\ m_{n+T} \end{pmatrix}}_{\boldsymbol{M}_T} &= \underbrace{\begin{pmatrix} \zeta_0^s & \cdots & \zeta_{T-1}^s & h_T^s \\ \zeta_1^s & \cdots & \zeta_T^s & 0 \\ \vdots & \iddots & 0 & 0 \\ \zeta_T^s & \cdots & 0 & 0 \end{pmatrix}}_{\boldsymbol{Z}_s} \underbrace{\begin{pmatrix} s_n \\ s_{n-1} \\ \vdots \\ s_{n-T} \end{pmatrix}}_{\boldsymbol{S}^g} \\ &+ \underbrace{\begin{pmatrix} \zeta_1^q & \cdots & \zeta_{T-1}^q & \zeta_T^q \\ \zeta_2^q & \cdots & \zeta_T^q & 0 \\ \vdots & \iddots & 0 & \vdots \\ \zeta_T^q & \cdots & 0 & 0 \\ 0 & \cdots & 0 & 0 \end{pmatrix}}_{\boldsymbol{Z}_q} \underbrace{\begin{pmatrix} q_{n-1} \\ q_{n-2} \\ \vdots \\ q_{n-T} \end{pmatrix}}_{\boldsymbol{Q}^g} \\ &+ \underbrace{\begin{pmatrix} \zeta_0^q & & & \\ \zeta_1^q & \zeta_0^q & & \\ \vdots & & \ddots & \\ \zeta_T^q & \cdots & \cdots & \zeta_0^q \end{pmatrix}}_{\boldsymbol{L}_q} \underbrace{\begin{pmatrix} q_n \\ q_{n+1} \\ \vdots \\ q_{n+T} \end{pmatrix}}_{\boldsymbol{Q}^f}. \end{aligned} \tag{10}$$

The Markov parameters ζ_i^q and ζ_i^s are the impulse responses of the output signal m to q and s respectively and satisfy

$$m_n = \sum_{i=0} \zeta_i^s s_{n-i} + \sum_{i=0} \zeta_i^q q_{n-i}. \tag{11}$$

They could be achieved from the corresponding impulse responses in the ARMAX model. In Fig. 11, the impulse response of the output signal to the two input signals tends to 0 when $t > 35$ for LMC and $t > 110$ for CMC, so the time period T should be greater than 400 for LMC and 1100 for CMC in Eq. (10). If we want to get the control input signal $\boldsymbol{Q}^f$ in the next period, we must know the future output signal $\boldsymbol{M}_T$ which is also the expected output signal. The control targets of LMC and CMC are completely suppressing the noise, that is to say $\|\boldsymbol{M}_T\|_2^2 = 0$, thus $\boldsymbol{Q}^f$ could be written as

$$\boldsymbol{Q}^f = (-\boldsymbol{L}_q^+ \boldsymbol{Z}_q)\boldsymbol{Q}^g + (-\boldsymbol{L}_q^+ \boldsymbol{Z}_s)\boldsymbol{S}^g. \tag{12}$$

Here $\boldsymbol{L}_q^+$ is the pseudo-inverse of matrix $\boldsymbol{L}_q$ because matrix $\boldsymbol{L}_q$ does not have an inverse matrix. Equation (12) defines a linear dynamic system where the input is the noise and control signal in the previous period, and the output is the control signal in the next period, so the compensator is also called a feed-forward controller. In the pseudo-inverse solution, the tolerance value needs to be set. The principle of tolerance setting is that the reciprocal of all singular values of the matrix $\boldsymbol{L}_q$ are greater than the tolerance value. However, the amplitude of the impulse response of the output signal to the input noise signal in the compensator increases as the tolerance decreases. In other words, growth of the amplitude of the control signal might improve the control cost. If the tolerance value is not considered, the performance of the compensator could be

better for a longer time period. Meanwhile, it could take more time to completely suppress the noise. The tolerance value is set to 0.15 for both LMC and CMC, and the time period is set to $t = 100$ and $t = 180$ for LMC and CMC respectively.

Figure 12(a) shows the impulse response of the output signal to the noise signal for the close-loop and open-loop systems. The dashed line represents the open-loop system, and the solid line represents the closed-loop system. Compared with the output signal without the controller, the response amplitude of the output signal decreases significantly after applying the controller, and tends to 0. Figure 12(b) shows the impulse response of the output signal with the controller to the noise signal, which is also the required control input signal for the closed-loop system. It can be seen that the control input signal decreases rapidly from the maximum value at the beginning, and then exhibits a damped oscillation and finally decays to 0.

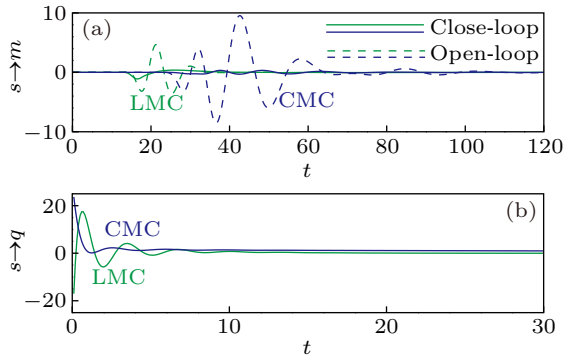


Fig. 12. The impulse response of output to input in LMC and CMC. (a) Impulse response of m to s; (b) impulse response of q to s.

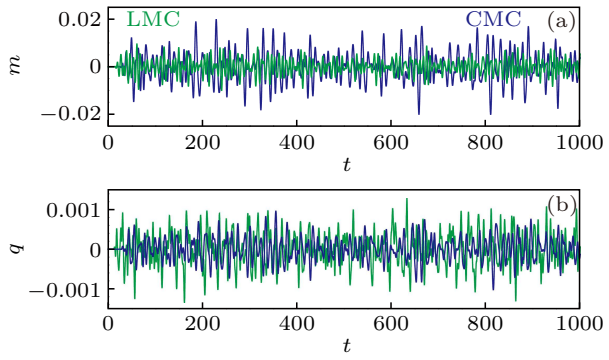


Fig. 13. Outputs of the open-loop system and close-loop system in LMC and CMC. (a) Open-loop system; (b) close-loop system.

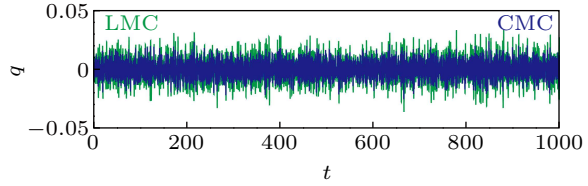


Fig. 14. Control inputs of the close-loop system.

Figure 13 shows the output signals obtained in the open-loop and close-loop systems. The signals in Fig. 13(a) from the open-loop system are the original filtered signals. The amplitude of the signal for LMC is less than that for CMC because the the location of S_2 for CMC is downstream that for LMC. Although the peak amplification rate for case B is much less that for case A, the measurements in local regions still grow along the flow direction. It can be seen that the pulsation amplitude of the output signal is reduced by 86.5% and 95.3% for LMC and CMC respectively after applying the controller.

4.4. Comparison

Figure 15 shows the perturbation energy $\mathcal{E} = \int_\Omega 0.5(u'^2 + v'^2)\mathrm{d}V$ of the entire liquid metal flow system varying with the evolution time for different control strategies. The black line, red line, green line and blue line represent the perturbation energy for NC, BFC, LMC and CMC respectively. All controls are turned on at $t = 2000$. We could find that the magnitude of the perturbation energy in the liquid metal flow could be reduced once the electromagnetic actuators are turned on. The average value of the perturbation energy in the time period of $t = 2500$–3500 is reduced by 54.9%, 97.4%, and 99.8% for BFC, LMC and CMC respectively. We could observe the profiles of NC and LMC have some overlap parts at beginning, and this phenomenon also exists for BFC and CMC. As discussed above, there exists a time interval for the response of the output signal to the input signal. We know the control targets of LMC and CMC are completely suppressing the noise, but the perturbation energy could not be suppressed completely. However, the magnitude of the perturbation energy could be reduced by 2 orders in LMC, and 3 orders in CMC. The inherent properties of amplification are responsible for this phenomenon. The sensor S_2 just could measure the local perturbation energy, and perturbations in other parts also be amplified. BFC could change the amplification features of the liquid metal BFS flow, and the linear control model could reduce the magnitude of the perturbation energy of whole liquid metal BFS flow. At least, CMC could achieve a better suppression of the perturbation energy compared with BFC and LMC. Since CMC is the combination of BFC and LMC, we could adjust the instability in the liquid metal BFS flow by turning on or turning off some actuators.

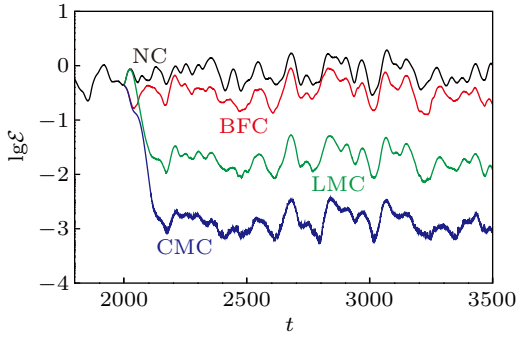


Fig. 15. Variations of the perturbation energy of the whole system for different control strategies.

5. Conclusion

To summarize, TEA and SEA could be applied to adjust the perturbation energy in the liquid metal BFS flow. Setting SEA in both PSB and SSB could amplify the magnitude of the perturbation energy, while combination of TEA, SEA (only acting on SSB) and two sensors could suppress the amplification of the perturbation energy. These results manifest that the electromagnetic actuators have the satisfied regulation effects on the perturbation energy in the liquid metal BFS flow, and the strategy of CMC could be commendably applied to engineering.

Acknowledgment

Project supported by the National Natural Science Foundation of China (Grant No. U2141246).

References

[1] Deng Y G, Jiang Y and Liu J 2021 *Appl. Therm. Eng.* **193** 117021
[2] Heinzel A, Hering W, Konys J, Marocco L, Litfin K, Müller G, Pacio J, Schroer C, Stieglitz R, Stoppel L, Weisenburger A and Wetzel T 2017 *Energy Technol.* **5** 1026
[3] Kirillov P L 2018 *Atom. Energy* **124** 238
[4] Miner A and Ghoshal U 2004 *Appl. Phys. Lett.* **85** 506
[5] Li P P and Liu J 2011 *Appl. Phys. Lett.* **99** 094106
[6] Panchadar K, West D, Taylor J A and Krupenkin T 2019 *Appl. Phys. Lett.* **114** 093901
[7] Kherbeet A S, Safaei M R, Salman B H, Mohammed H A, Ahmed H E, Alawi O A and Khazaai M T 2016 *Int. Commun. Heat Mass Transf.* **76** 237
[8] Iwai H, Nakabe K and Suzuki K 2000 *Int. J. Heat Mass Transf.* **43** 457
[9] Juste G L, Fajardo P and Guijarro A 2016 *Phys. Fluids* **28** 074106
[10] Blackburn H M, Barkley D and Sherwin S J 2008 *J. Fluid Mech.* **603** 271
[11] Ghia K N, Osswald G A and Ghia U 1989 *Int. J. Numer. Methods Fluids* **9** 1025
[12] Barkley D, Gomes M G M and Henderson R 2002 *J. Fluid Mech.* **473** 167
[13] Lanzerstorfer D and Kuhlmann H C 2012 *J. Fluid Mech.* **693** 1
[14] Kaiktsis L, Karniadakis G E and Orszag S 1996 *J. Fluid Mech.* **321** 157
[15] Velazquez A, Arias J R and Mendez B 2008 *Int. J. Heat Mass Transf.* **51** 2075
[16] Mehrez Z, Bouterra M, Cafsi A E, Belghith A and Quere P L 2009 *Heat Mass Transf.* **46** 107
[17] Oyakawa K, Taira T, Senaha I and Nosoko T 1995 *Int. Commun. Heat Mass Transf.* **22** 343
[18] Li Z Y, Guo S, Bai H L and Gao N 2019 *Int. J. Heat Mass Transf.* **130** 240
[19] Hilo A K, Talib A R A, Iborra A A, Sultan M T H and Hamid M F A 2020 *Energy* **190** 116294
[20] Kumar S and Vengadesan S 2018 *Numer. Heat Tranf. A-Appl.* **73** 366
[21] Modestov M, Kolemen E, Fisher A E and Hvasta M G 2018 *Nucl. Fusion* **58** 016009
[22] Hvasta M G, Kolemen E, Fisher A E and Ji H 2018 *Nucl. Fusion* **58** 016022
[23] Cho S and Hong S H 1998 *J. Phys. D-Appl. Phys.* **31** 2754
[24] Albrecht T, Stiller J, Metzkes H, Weier T and Gerbeth G 2013 *Eur. Phys. J.-Spec. Top.* **220** 275
[25] Huang T D, ZHOU B M, Tang Z L and Zhang F 2017 *Phys. Fluids* **29** 074105
[26] Hervé A, Sipp D, Schmid P J and Samuelides M A 2012 *J. Fluid Mech.* **702** 26
[27] Gautier N and Aider J L 2014 *J. Fluid Mech.* **759** 181
[28] Ljung L 1999 *System Identification: Theory for the User*, 2nd edn. (Prentice Hall)
[29] Du Y Q and Karniadakis G E 2000 *Science* **288** 1230
[30] Rossi L and Thibault J P 2002 *J. Turbul.* **3** N5
[31] Sipp D and Schmid P J 2016 *Appl. Mech. Rev.* **68** 020801
[32] Blackburn H M, Lee D, Albrecht T and Singh J 2019 *Comput. Phys. Commun.* **245** 106804
[33] Barkley D, Blackburn H M and Sherwin S J 2008 *Int. J. Numer. Meth. Fluids* **57** 1435
[34] Mao X R 2015 *J. Fluid Mech* **771** 229